A Novel Soft Switching Bidirectional DC–DC Converter Using Magnetic and Capacitive Hybrid Power Transfer

Masanori Ishigaki, *Member, IEEE*, Jongwon Shin, *Member, IEEE*, and Ercan M. Dede, *Member, IEEE*

***Abstract*—This paper proposes a new bidirectional dc–dc converter capable of improving the convenience and modularity of the dc power grid system. By the unique operation of the LC resonant transformer, the proposed converter achieves bidirectional power control with only two switches. Also, the resonant transformer drives the soft switching turn-on and turn-off over a wide power range. Hence, the circuit has high potential to downsize the converter by exploiting high frequency and simplicity. This paper provides the operating principle and the experimental verification of the proposed circuit. A prototype was fabricated by using a simple and high-density printed circuit board ($\geq$10 W/cc). It is verified that the circuit resonant operation successfully drives bidirectional power control with high efficiency ($\geq$92%). An application example is also provided for dc grid system integration.**

***Index Terms*—DC–DC power conversion, energy storage, power distribution, resonant power conversion.**

I. Introduction

With the rapid development of electric energy storage device technologies, dc power systems are becoming widely used in various applications. In electricity infrastructure, large energy storage devices such as Li-ion batteries promote distributed renewable energy sources, which include photovoltaic (PV) power systems, wind generator systems, and fuel cell systems in microgrids [1], [2]. In transportation as well, electrification is a main stream of the vehicle industry for improving fuel economy and reducing environmental burdens. Nowadays, there are many themes for future transportation research related to electric energy storage systems and batteries, e.g., [3]–[9]. Regarding recharge capability, electric energy storage devices such as batteries or supercapacitors require bidirectional dc–dc energy conversion to optimize system efficiency [10]–[15], [17]–[20]. Therefore, cost reduction and downsizing of bidirectional dc–dc converters is actively sought to sustain the growth of system performance. To achieve this goal, power electronics technologies are being developed using several approaches.

Manuscript received June 6, 2016; revised September 23, 2016; accepted October 24, 2016. Date of publication November 1, 2016; date of current version April 24, 2017. Recommended for publication by Associate Editor C. T. Rim.

The authors are with Toyota Research Institute of North America, Toyota Motor Engineering and Manufacturing North America, Ann Arbor, MI 48105 USA (e-mail: masanori.ishigaki@toyota.com; jongwon.shin@toyota.com; eric.dede@toyota.com).

Color versions of one or more of the figures in this paper are available online at http://ieeexplore.ieee.org.

Digital Object Identifier 10.1109/TPEL.2016.2624024

At the semiconductor level, silicon carbide (SiC) devices are now well known as a game changing technology for middle-to-high voltage applications, e.g., >600-V dc grid. The lateral gallium nitride (GaN) FET is also a promising device for improving the power density and efficiency of low-voltage circuit topologies through downsizing of passive components and by increasing the operating frequency to the megahertz range [21]–[24]. Regarding circuit topologies, soft switching technology is widely adopted to downsize passive devices with high-frequency operation [25]–[27]. Several integrated circuit topologies are presented for a variety of specific applications [28]–[30].

This paper is focused on a new soft-switching dc–dc converter capable of controlling bidirectional power flow using only two switches. With LC resonance technology, the proposed circuit achieves the integration of soft switching and bidirectional power control functions. Thus, this circuit is able to downsize the semiconductor footprint by exploiting high-frequency operation in combination with a smaller number of devices and reduced volume of passives. From a system control prospective, the proposed circuit is able to control output power directly by adjusting the on-time of the switches. This simplifies the controller and reduces the dc–dc converter cost.

The remainder of this paper is organized as follows. In Section II, an overview of the dc grid system and dc–dc converter technologies is provided. The basic functions and design of the proposed circuit are shown with a theoretical analysis in Section III. In Section IV, the static characteristics and conversion efficiency are verified by the experimental results; the experimental results also confirm the system operation as a rechargeable source power controller. Conclusions are provided in Section V.

II. DC Grid System and DC–DC Converter

Fig. 1 illustrates an example of a low-voltage electrical energy storage system. The system has several sources and loads with two voltage buses, i.e., $V_1 = 12$ V and $V_2 = 48$ V. The low-voltage grid, V_1, connects three energy storage devices for several purposes. The lithium (Li)-ion battery is connected as the main energy storage device. And a lead-acid battery is connected to the system for the purpose of cold temperature stability. The electric double-layered capacitor (EDLC) is a support device that provides or absorbs transient power to protect both batteries

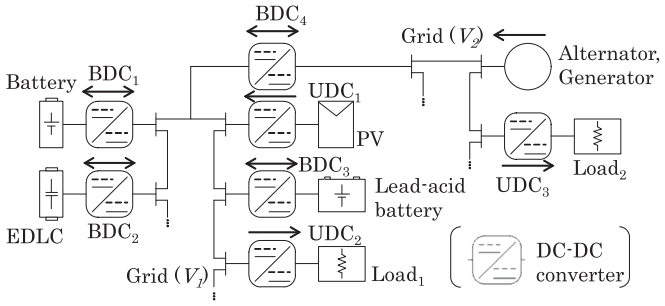

Fig. 1. Example of a dc grid system. Loads and sources are connected to the grid through unidirectional dc–dc converters, and all rechargeable components are connected to the grid through bidirectional dc–dc converters.

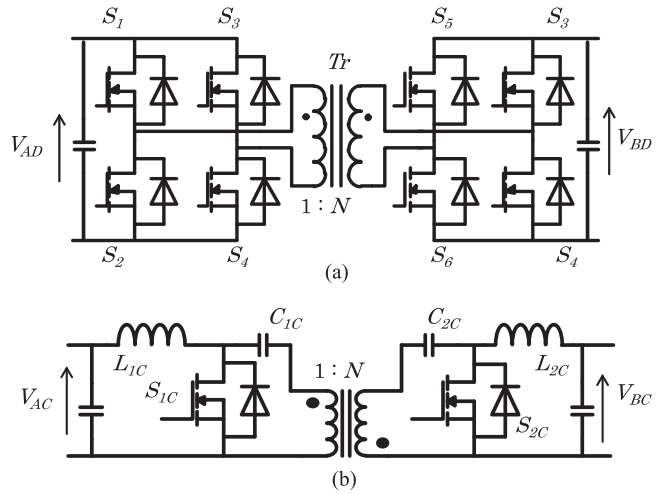

Fig. 2. Conventional bidirectional dc–dc converters. (a) Dual-active-bridge bidirectional dc–dc converter (DAB). (b) Bidirectional Cúk dc–dc converter.

from degradation. Each power source has a bidirectional dc–dc converter, BDC_1, BDC_2, BDC_3, to manage the grid power and to control the state of charge of the energy source. A PV solar cell is connected through a unidirectional dc–dc converter, UDC_1, with maximum power point tracking control, and a load, Load_1, is connected though a unidirectional converter, UDC_2. The other grid, V_2, has a motor/generator with inverter drive, and a high voltage load, Load_2, is connected through unidirectional dc–dc converter, UDC_3. Both grids are connected by a bidirectional dc–dc converter, BDC_4, to maximize system functionality.

In this example, the dc grid system requires a number of dc–dc converters for optimizing the energy flow and maintaining stability. In particular, a bidirectional dc–dc converter is necessary for energy storage to not only improve efficiency but to also protect the sources from overcharge or undercharge. If the sources have different ground levels, the dc–dc converters need to provide isolation or a level shift. Additionally, these dc–dc converters must provide high current capability due to the low-voltage grid structure.

Fig. 2 shows two examples of conventional isolated bidirectional dc–dc converters. Both converters are capable of controlling bidirectional power flow regardless of the magnitude of the terminal voltages. Fig. 2(a) shows a well-known bidirectional dc–dc converter topology that uses a bridge circuit, which called a dual active bridge (DAB)[10]. Switches S_1–S_4 and S_5–S_8 make two H-bridge circuits for applying rectangular voltage to the transformer and control bidirectional power by adjusting the phase of the rectangular voltage. By the phase-shifted current, the switches are able to reduce loss by soft switching over a wide power range. However, in practice, the operating frequency is limited by the dead time, which is necessary for the short-circuit protection of the bridge circuit. Additionally, bridge-type circuits make the system complicated due to the complex gate drive circuits and controller needed to drive the eight switches.

Fig. 2(b) shows an another example of a bidirectional dc–dc converter [15]. This v-er has only two switches for the bidirectional operation. However, the operating frequency is limited by the switching loss due to the hard-switching operation. An auxiliary circuit may reduce switching loss by soft switching, though this increases the complexity and the cost [16]. In addition, the operation current is limited by the series-connected capacitors C_{1c} and C_{2c}.

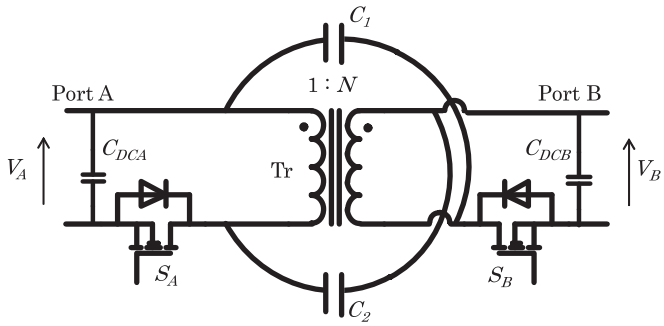

Fig. 3. MagCap: Proposed bidirectional dc–dc converter. Both of input and output ports are connected by the symmetrical circuit contains two MOSFETs, a transformer (magnetic device), and capacitors (capacitive device).

III. Proposed DC–DC Converter: MagCap

In this section, a novel dc–dc converter topology is proposed. The principle of operation is explained, and a theoretical analysis for transmitting power is provided.

A. Circuit Topology

Fig. 3 shows the proposed bidirectional dc–dc converter. Both ports A and B connect to a winding of the transformer, Tr, and a MOSFET, $\mathrm{S_A}$ or $\mathrm{S_B}$, in series. Additionally, two capacitors, C_1 and C_2, are connected across the transformer terminals. The transformer that has a winding turn ratio N is designed as a loosely coupled transformer to design the leakage inductance, L_l. The capacitors C_1, C_2 and the leakage inductance L_l create LC resonance, and the device output capacitance C_{oss} also creates another LC resonance with L_l. These resonances drive the soft switching of the MOSFETs and help suppress bias issues associated with the transformer. The proposed circuit applies constant off-time switching and controls power flow by adjusting the on-time of the MOSFETs. Hence, the operating

TABLE I
COMPARISON OF THE STRUCTURAL AND FUNCTIONAL FEATURES OF DC–DC CONVERTERS

Circuit	DAB	Cúk	MagCap
Number of MOSFETs	8	**2**	**2**
Passive devices	**Transformer**	Series-connected transformer and capacitor	Parallel-connected transformer and capacitor
Soft switching	**Yes**	No	**Yes**
Controlled objective	**Power** $= f$**(phase)**	Voltage $= f$(duty)	**Power** $= f$**(on-time)**

frequency is variable in this circuit. The circuit is symmetrical, which leads to easy bidirectional operation.

This proposed circuit transmits bidirectional power through both magnetic and capacitive passive devices and, accordingly, is named and referred to as "MagCap" from this point forward. Table I provides a comparison between the proposed converter and the conventional circuits shown in Fig. 2. The MagCap circuit topology provides the function of a DAB with fewer components similar to the Cúk circuit topology. However, in contrast with the Cúk converter, the MagCap is capable of handling high current by connecting the transformer and capacitor in parallel. Input and output terminals are isolated by both the transformer and resonant capacitors. The isolation voltage between the input and output terminals are determined by the voltage rating of the capacitors. Generally, ceramic capacitors with kilovolt-order voltage rating and nanofarad-order capacitance are easily found in the market [31]. These capacitors meet both functional and basic insulation as defined in IEC60950 Class I. Furthermore, if MagCap is utilized as a level shifter such as in active battery cell balancing applications in dc power systems [32], [33], low-equivalent-series-resistance (ESR) capacitors can be employed based on the system voltage requirements.

The following sections describe the principle of operation and theoretical analysis of power control.

B. Principle of Operation

Fig. 4 illustrates the operation of the MagCap circuit. Fig. 4(a) shows the equivalent circuit with parasitic parameters. The parameter of the transformer is broken down to the exciting inductance $L_{\rm m}$ and the leakage inductance L_l. The capacitances $C_{\rm ossA}$ and $C_{\rm ossB}$ are the output capacitance of the MOSFET. Equations (1)–(3) show three LC resonances for MagCap operation in a period:

$$\omega_1 = \frac{1}{\sqrt{L_{\rm lB}(C_1//C_2)}} \tag{1}$$

$$\omega_2 = \frac{1}{\sqrt{L_{\rm lA}(C_1//C_2)}} \tag{2}$$

$$\omega_3 = \frac{1}{\sqrt{L_{\rm lA}(C_{\rm ossA}//N^2C_{\rm ossB})}} \tag{3}$$

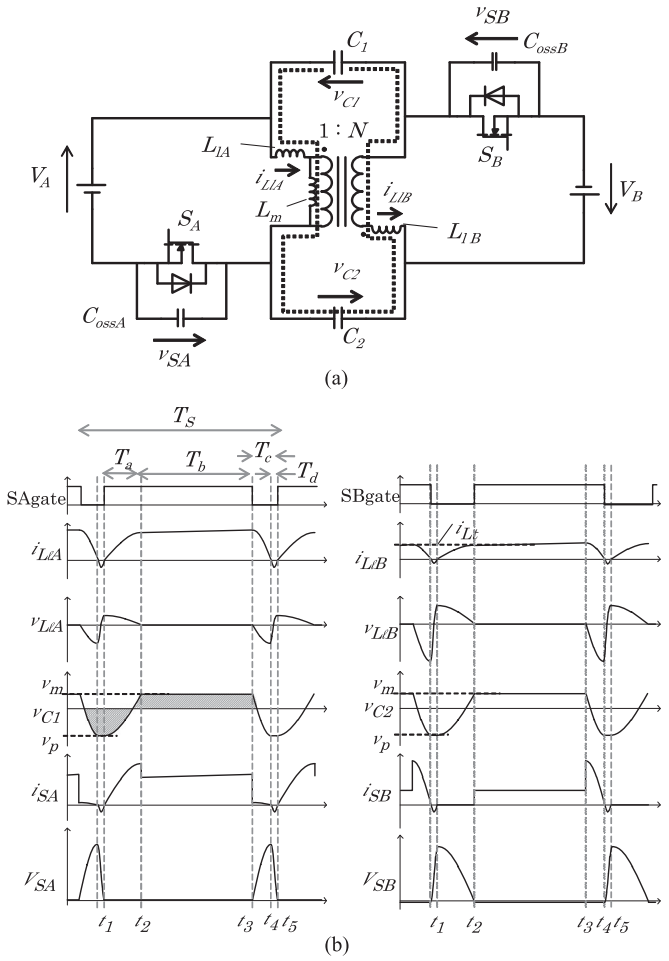

Fig. 4. Equivalent circuit and ideal waveforms. (a) Equivalent circuit of the MagCap. C_{S1} and C_{S2} describe the equivalent output capacitors of MOSFET, L_{l1} and L_{l2} are the leakage inductance, and L_m is the excitation inductance of the transformer. (b) Ideal waveforms.

where $L_{\rm lA}$ and $L_{\rm lB}$ are the equivalent leakage inductances determined by the following equation:

$$L_{\rm lA} = 2L_l = \frac{L_{\rm lB}}{N^2}. \tag{4}$$

Fig. 4(b) shows the ideal waveform of the MagCap when power is transmitted from port A to port B with $N = 2$. The operation is divided into four modes. Using the resonant frequencies shown in (1)–(3), time definition of these modes T_a to T_d can be written as follows:

$$T_a = t_2 - t_1 = \frac{\pi}{2\omega_1} \tag{5}$$

$$T_b = t_3 - t_2 = T_{\rm on} - T_a \tag{6}$$

$$T_c = t_4 - t_3 = \frac{\pi}{2\omega_2} \tag{7}$$

$$T_d = t_5 - t_4 = \frac{\pi}{\omega_3} \tag{8}$$

$$T_{\rm off} = T_c + T_d. \tag{9}$$

$T_{\rm on}$ and $T_{\rm off}$ are the on-time and the off-time of $\rm S_A$ in Fig. 4(b) to control the transmitting power from port A to port B. The same

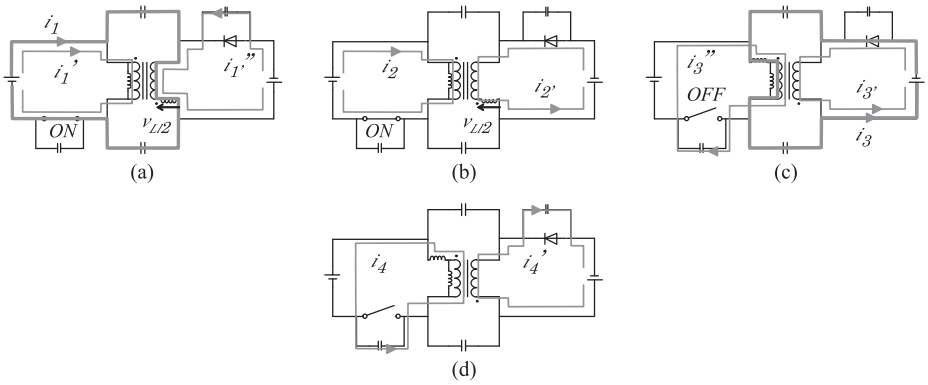

Fig. 5. Operation of each mode. (a) Mode 1 ($t_1 \le t \le t_2$): excite the transformer and charge the capacitors. (b) Mode 2 ($t_2 \le t \le t_3$): transmit the power through transformer. (c) Mode 3 ($t_3 \le t \le t_4$): transmit power to discharge capacitors. (d) Mode 4 ($t_4 \le t \le t_5$): discharge $C_{\rm oss}$ of $\rm S_A$ for ZVS turn-on.

algorithm is utilized for $\rm S_B$ to control reverse power direction. Note that the off-time $T_{\rm off}$ is fixed by the inductance and the capacitances by (2) and (3), while on-time $T_{\rm on}$ is an adjustable value. Fig. 5 illustrates the operation of each of the four modes in terms of the current path on the circuit. From (10)–(24), it is possible to derive the transmitted power $P_{\rm dd}$ along with describing the details of each mode.

1) Mode 1: Charge Passive Devices: In the first mode shown in Fig. 5(a), L_l, C_1, and C_2 store the energy by the source connected in port A through $\rm S_A$. When $\rm S_A$ is turned ON, the capacitor voltages v_{C1} and v_{C2} are changed from v_p to v_m by the resonant current flow i_1. The current $i_{\rm LlB}$ of the leakage inductance $L_{\rm lB}$ is described as

$$i_{\rm LlB} = i_{\rm Lt} \sin \omega_1 (t - t_1). \tag{10}$$

The value $i_{\rm Lt}$ is the amplitude of this resonance, which can be solved by the energy balance of the switching cycle. In this mode, another current i_1' flows through S_A. The relation between $i_{\rm LlB}$ and i_1' is determined by the winding ratio N, so the device current $i_{\rm sA}$ is described as

$$i_{\rm SA} = i_{\rm LlB} + i_1' = (1 + N) i_{\rm LlB}. \tag{11}$$

The current of leakage inductor $i_{\rm LlB}$ reaches its peak value $i_{\rm Lt}$ at $t = t_2$.

2) Mode 2: Transmit Power Through Transformer: Fig. 5(b) shows the operation of the magnetic power transmission mode. When v_{C1} and v_{C2} reach to v_m, the voltage relation satisfies the following equation:

$$V_A + V_B - v_{C1} - v_{C2} = 0. \tag{12}$$

Then, both of v_{C1} and v_{C2} are clamped by the input voltages, and the operation mode shifts from mode 1 to mode 2. The clamped voltage can be described as

$$v_{C1} = v_{C2} = v_m = \frac{V_A + V_B}{2}. \tag{13}$$

The leakage inductor continuously draws the power from V_A and transmits it to V_B by $i_{\rm Lt}$. The transmitted power P_2 is calculated by

$$P_2 = \int_{t_2}^{t_3} i_{\rm Lt} V_B \, dt = \frac{1}{T_s} i_{\rm Lt} V_B T_b. \tag{14}$$

The switch $\rm S_B$ is turned ON during this period to reduce the conduction loss like synchronous rectification.

3) Mode 3: Transmit Power Through Capacitors: Fig. 5(c) shows the operation of capacitive power transmission mode. When $\rm S_A$ is turned OFF at $t = t_3$, current flows rotational symmetry through 180° from mode 1. The energy stored by the capacitors and leakage inductance from port A during the mode 1 is released to port B through the flow i_3 and i_3'. The leakage current $i_{\rm LlA}$ is described as

$$i_{\rm LlA} = N i_{\rm Lt} \cos \omega_2 (t - t_3) \tag{15}$$

and the device current $i_{\rm sB}$ is described as

$$i_{\rm SB} = -(1 + N)/N i_{\rm LlA}. \tag{16}$$

By using (16), the transferred power P_3 is calculated by

$$P_3 = \frac{1}{T_s} \int_{t_3}^{t_4} V_B i_{\rm SB} \, dt = \frac{i_{\rm Lt}(1 + N) V_B}{\omega_2 T_s}. \tag{17}$$

Similar to mode 2, $\rm S_B$ is able to be turned ON for reducing the conduction loss in this mode. During this mode, the output capacitor $C_{\rm ossA}$ is charged by the current flow i_3''. When the capacitance of C_1 and C_2 is larger than $C_{\rm ossA}$ and $C_{\rm ossB}$, the voltage relation of the circuit can be described simply as

$$\begin{aligned} V_{\rm SA} - V_A - V_B &= -(v_{c1} + v_{c2}) \\ &= -L_{\rm lA} \frac{di_{\rm LlA}}{dt} \\ &= N i_{\rm Lt} L_{\rm lA} \omega_2 \sin \omega_2 (t - t_3). \end{aligned} \tag{18}$$

From (7) and (18), device voltage $V_{\rm SA}$ reaches the peak at $t = t_4$. The peak value of the device voltage $V_{\rm SA(p)}$ is described as

$$V_{\rm SA(p)} = N i_{\rm Lt} L_{l1} \omega_2 + V_A + V_B. \tag{19}$$

4) Mode 4: Discharge $C_{\rm ossA}$: Fig. 5(d) illustrates the charging and discharging operation for $C_{\rm ossA}$ and $C_{\rm ossB}$. When $i_{\rm LlA}$ reaches zero and $\rm S_B$ is turned OFF at $t = t_4$, the resonant operation shown in (15) is stopped by the body diode of $\rm S_B$. Instead, the leakage inductor creates another resonant current shown as i_4 and i_4' with the output capacitors $C_{\rm ossA}$ and $C_{\rm ossB}$. The current i_4' charges $C_{\rm ossB}$ and the voltage of $V_{\rm SB}$ reaches to its peak

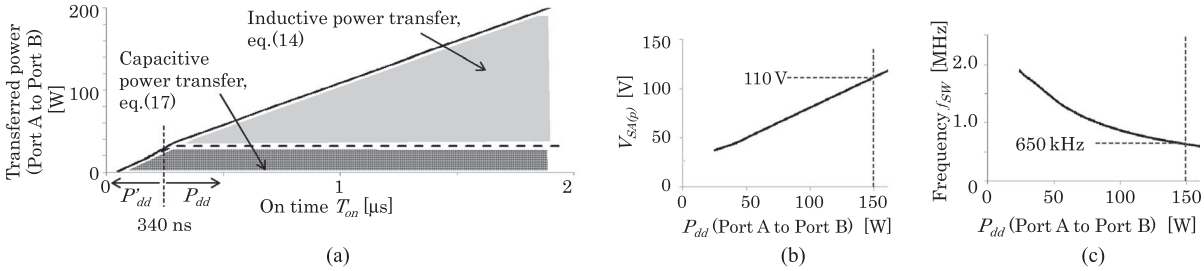

Fig. 6. Relations of the transmitting power $P_{\rm dd}$, control value $T_{\rm on}$, the device peak voltage $V_{\rm SA(p)}$, and operating frequency $f_{\rm sw}$. (a) $T_{\rm on}$ versus transmitted power $P_{\rm dd}$. (b) $P_{\rm dd}$ versus $V_{\rm SA(p)}$. (c) $P_{\rm dd}$ versus $f_{\rm sw}$.

$V_{\rm SB(p)}$ at $t = t_5$ as follows:

$$V_{\rm SB} = NC_x \frac{\left[V_{\rm SA(p)} + \frac{V_B}{N} - V_A\right]\left[1 - \cos\omega_3(t - t_4)\right]}{N^2 C_{\rm ossB}} \quad (20)$$

$$V_{\rm SB(p)} = 2C_{\rm ossA} \frac{NV_{\rm SA(p)} + V_B - NV_A}{C_{\rm ossA} + N^2 C_{\rm ossB}} \quad (21)$$

where

$$C_x = \frac{C_{\rm ossA} N^2 C_{\rm ossB}}{C_{\rm ossA} + N^2 C_{\rm ossB}}. \quad (22)$$

The current flow i_4 also discharges $C_{\rm ossA}$, and the voltage $V_{\rm SA}$ drops as per the following equation:

$$V_{\rm SA} = C_x \frac{\left[V_{\rm SA(p)} + V_B/N - V_A\right]\left[1 - \cos\omega_3(t - t_4)\right]}{C_{\rm ossA}} + V_{\rm SA(p)}. \quad (23)$$

If (23) satisfies $V_{\rm SA} \le 0$ at $t = t_5$, $\rm S_A$ is able to turn ON with zero-voltage switching (ZVS). With the parameters, the ZVS condition is shown as

$$\frac{N^2 C_{\rm ossB} - C_{\rm ossA}}{N^2 C_{\rm ossB}} \ge \frac{V_A - V_B/N}{V_{\rm SA(p)}}. \quad (24)$$

The left-hand side of (24) is determined by the circuit design, and it is equal to zero when the circuit is implemented with the same devices for $\rm S_A$ and $\rm S_B$ and $N = 1$. In this case, the right-hand side of (24) decides whether $\rm S_A$ is able to achieve ZVS operation. This is guaranteed when the circuit transfers power from low voltage to high voltage. However, $V_{\rm SA}$ is not able to reach zero at $t = t_5$ when V_A is higher than V_B. The remaining energy $1/2 C_{\rm ossA} {V_{\rm SA}}^2$ will be wasted when $\rm S_A$ turns ON.

C. Theoretical Analysis on Transmitting Power

The total transmitting power, $P_{\rm dd} = P_2 + P_3$, is determined by calculating the value of $i_{\rm Lt}$ used in (14) and (17). In mode 1, the energy stored C_1 and C_2 is moved to the inductor L_{l2} by resonance. The relationship between $i_{\rm Lt}$ and v_p, v_m is described as follows:

$$\frac{1}{2}(C_1 + C_2)v_p^2 = \frac{1}{2}L_l i_{\rm Lt}^2 + \frac{1}{2}(C_1 + C_2)v_m^2 \quad (25)$$

$$i_{\rm Lt} = \frac{v_m - v_p}{\omega_1 N L_{l1}}. \quad (26)$$

As highlighted by the dashed line in Fig. 4(a), C_1, C_2, and the transformer create a loop. Thus, the average of the capacitor voltages that are shown as the shaded areas in Fig. 4(b) is zero

$$\int_0^{T_s} v_{c1}\,dt = \int_0^{T_s} v_{c2}\,dt = 0. \quad (27)$$

From (1)–(9) and (27), the negative peak voltage of the capacitors v_p is described as

$$v_p = -v_m \frac{(N+1)(\pi - 2) + 2\omega_1 N T_b}{2(N+1) + 2N\frac{\omega_1}{\omega_3}\pi}. \quad (28)$$

The positive peak voltage of the capacitors v_m is calculated by (13). By (26), (13), and (28), the transmitting power $P_{\rm dd}$ is described as follows:

$$\begin{aligned} P_{\rm dd} &= P_2 + P_3 \\ &= \frac{i_{\rm Lt} V_B}{T_s}(T_b) + \frac{i_{\rm Lt}(1+N)V_B}{\omega_2 T_s} \\ &= \left(\frac{V_A + V_B}{2}\right)\frac{V_B(\omega_2 T_b + N + 1)}{T_s \omega_1 \omega_2 N L_{lA}} \\ &\quad \left(1 + \frac{(N+1)(\pi - 2) + 2\omega_1 N T_b}{2(N+1) + 2N\frac{\omega_1}{\omega_3}\pi}\right). \end{aligned} \quad (29)$$

From (29), $P_{\rm dd}$ is a monotonically increasing function for $T_b = T_{\rm on} - T_c - T_d$. Thus, this circuit is able to control the transmitting power by adjusting the on-time with constant off-time control.

TABLE II
SIMULATION PARAMETERS

Parameter	Symbol	Value
Turn ratio	N	1
Leakage inductance	$L_{\rm lA}$, $L_{\rm lB}$	0.62 μH
Resonant capacitor	C_1, C_2	33 nF
Output capacitor	$C_{\rm ossA}$, $C_{\rm ossB}$	1 nF

D. Simulation Result

Fig. 6 shows the simulation result of (29), which describes the relations of $P_{\rm dd}$, $V_{\rm SA(p)}$, and switching frequency $f_{\rm sw}$. Table II shows the parameters for the simulation. The transformer has leakage inductance $L_{\rm lA} = 1.2$ μH, and the capacitance $C_{\rm ossA}$ and $C_{\rm ossB}$ set as constant values. The resonant frequencies are

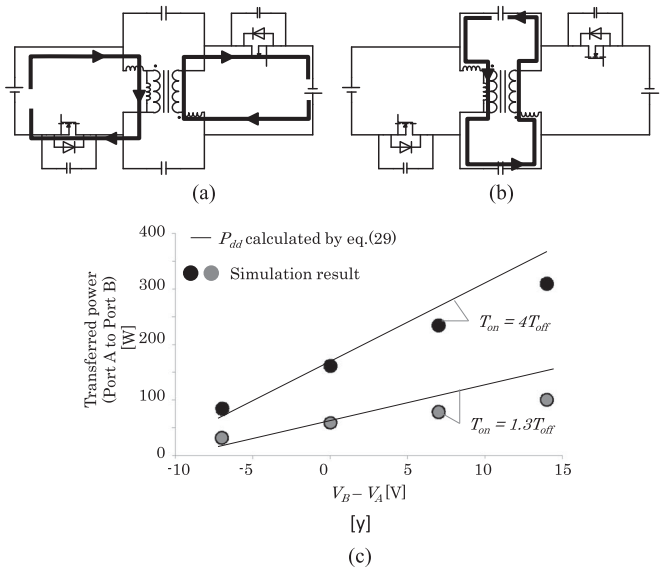

Fig. 7. Analysis of circulating current by the voltage difference. (a) Circulating current path of mode 1 and mode 3 at $V_A \leq V_B$. (b) Circulating current path of mode 2 at $V_A \leq V_B$. (c) Transmitting power analysis for voltage variation. Each voltage set at $V_A = 14$ V, and 7 V $\leq V_B \leq 28$ V.

calculated by (1)–(3):

$$\frac{\omega_1}{2\pi} = \frac{\omega_2}{2\pi} = \frac{1}{2\pi\sqrt{L_{l2}(C_1//C_2)}} = 1.1\,\text{MHz} \quad (30)$$

$$\frac{\omega_3}{2\pi} = \frac{1}{2\pi\sqrt{L_{\text{lA}}C_{\text{ossA}}}} = 4.5\,\text{MHz}. \quad (31)$$

From (30) and (31), constant off-time T_{off} is calculated as 340 ns. Fig. 6(a) shows the relation of the transmitted power P_{dd} and T_{on}. P_{dd} is proportionally increased by T_{on} and reaches 150 W when $T_{\text{on}} = 1.25$ μs. Essentially, 20% of P_{dd} is transmitted by the capacitive mode. At $T_{\text{on}} \leq T_a \approx 250$ ns, T_{on} is not enough for i_{LlB} to reach the peak value at mode 1. In this case, the operation is similar to the capacitive power transfer shown in (17), the transmitted power P'_{dd} is approximately calculated as

$$P'_{\text{dd}} = \frac{1}{T_s}\int_0^{t_{\text{on}}} V_A i_{\text{SA}}\,dt. \quad (32)$$

Fig. 6(b) and (c) shows the behavior of the device peak voltage $V_{\text{SA(p)}}$ and operating frequency f_{sw}. $V_{\text{SA(p)}}$ is proportionally increased by P_{dd}, and f_{sw} is decreased by the power increase. In this design, $V_{\text{SA(p)}}$ reaches 110 V and f_{sw} is set to 630 kHz at $P_{\text{dd}} = 150$ W. From Fig. 6, it is verified that the transmitting power of the MagCap circuit is controllable by adjusting on-time in a linear fashion. To transmit the power form port B to port A, S_B adjusts on-time and S_A is used for synchronous rectification.

Fig. 7 shows the behavior of circulating current between input and output terminals. The circulating current occurs when V_A is not equal to V_B/N, which is similar to a conventional DAB converter [30]. Fig. 7(a) and (b) displays an example of the circulating current when $V_A \leq V_B/N$. Fig. 7(a) presents the dc bias caused by the circulating current in capacitive power transfer mode. Fig. 7(b) shows the circulating current path in magnetic power transfer mode. Note that the current in the lower voltage side increases, and the current in the higher voltage side decreases to balance the input and output power. The effect of the circulating current on transferred power is plotted in Fig. 7(c). Because capacitive power transfer is affected by the circulating current shown in Fig. 7(a), the actual value of transferred power is different from the calculated transferred power, per (29). This difference becomes more extreme with shorter on-time of the switch, especially in the capacitive power transfer mode. However, this difference is negligible when the voltage difference of the input and output voltages stays within a $\pm$ 50% range. In addition, design consideration is required to avoid the saturation of the transformer due to the circulating current.

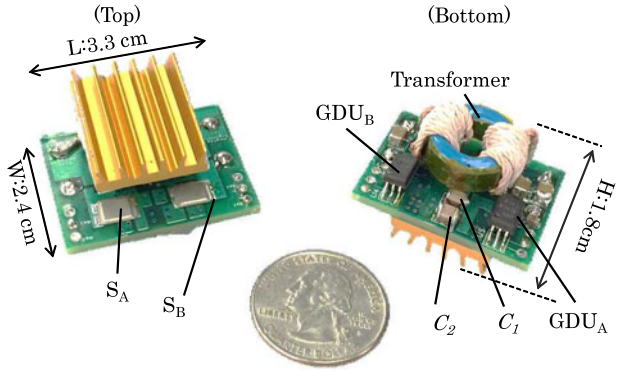

Fig. 8. Prototype of the MagCap circuit. The heat sink is floating to reveal in the picture.

TABLE III
SPECIFICATIONS OF THE EXPERIMENTAL CIRCUIT

Component	Symbol	Note
MOSFET	S_A, S_B	BSB165N15NZ3, 150 V, 16 mΩ (IPP075N15N3, 150 V TO-220 package for waveform measurement)
DC capacitor	C_{DCA}, C_{DCB}	50 μF
Core material	Tr	N87, R 16 x 9 x 6.5
Turn number	n_a, n_b	6 turns
Gap	g	0.1 mm
Excitation inductance	L_m,	5.3 μH
Leakage inductance	L_{lA},	1.23 μH
Resonant capacitor	C_1, C_2	TDK, 33 nF
Gate driver	GDU_A	ACPL-P343, 4 A peak
	GDU_B	inc. UVLO function

IV. EXPERIMENTAL RESULTS

A. Verification of the Operation

Fig. 8 shows a picture of the prototype circuit, and Table III describes the specifications of the circuit. The transformer uses a standard ferrite core and litz wire for this proof of concept, and 0.1-mm gap is inserted into the core for designing leakage inductance and removing the saturation risk shown in Fig. 7. An isolated gate driver is selected for GDU_A and GDU_B, which has 700-mW heat capacity and takes the driving power directly

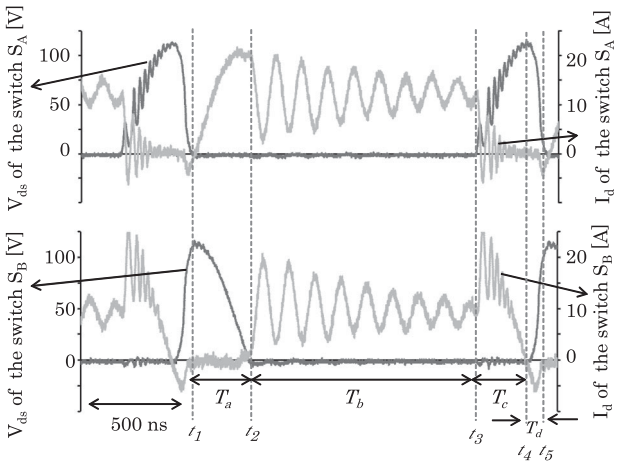

Fig. 9. Experimental waveforms at $V_A = V_B = 14\,V$, $P_{\rm dd} = 130$ W. Each voltage waveforms are measured by the differential voltage probe, and Rogowski coil is used for current waveforms measurement.

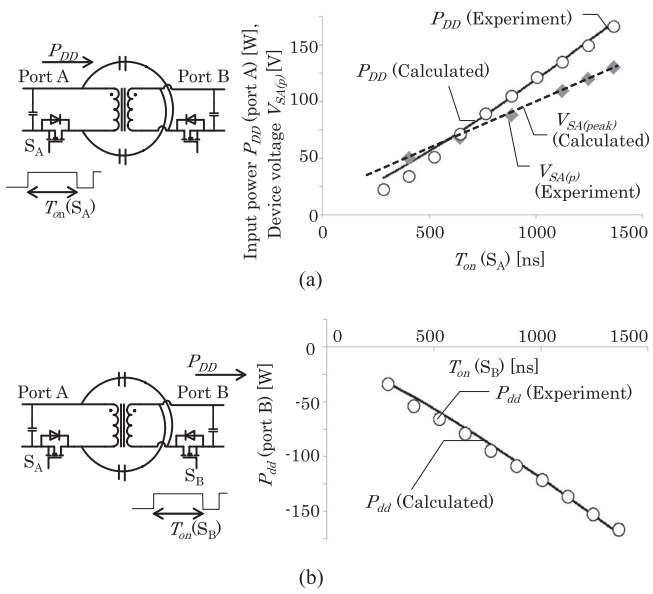

Fig. 10. Measured transmitting power at $V_A = V_B = 14$ V. (a) From port A to port B, S_A adjusts the on-time and S_B is used for synchronous rectification. (b) From port B to port A, S_B adjusts the on-time and S_A is used for synchronous rectification.

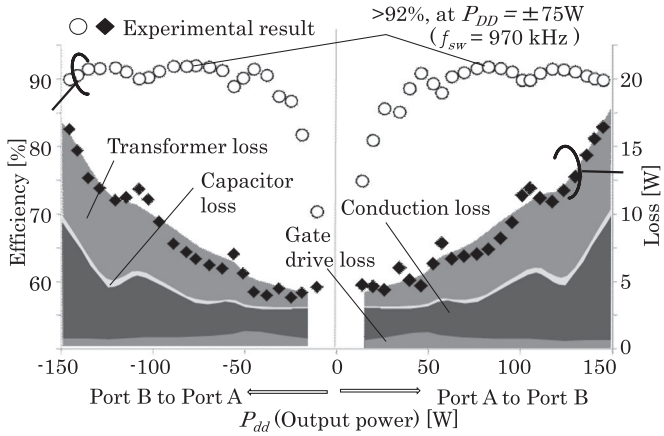

Fig. 11. Measured efficiency and loss at $V_A = V_B = 14$ V. X-axis is defined as output power for each direction. The contours are estimated by simulation.

from port A or port B. The size of the converter is approximately 15 cc including a heat sink for both devices.

Fig. 9 shows the experimental waveforms when power of 130 W is transmitted from V_A to V_B. To measure the current waveforms by using Rogowski coil, the MOSFETs in TO-220 are temporarily used. S_A turns ON with zero voltage and zero current at $t = t_1$ and turns OFF with zero voltage at $t = t_3$. The peak voltage of the MOSFETs reaches $V_{\rm SA(p)} = V_{\rm SB(p)} =$ 110 V. The stray inductance L_s of the MOSFET drives additional ringing. The oscillation during the period T_b is driven by series resonance of L_s, C_1 and C_2, and another oscillation is driven by the resonance between L_s and $C_{\rm ossA}$. Note that both ringings are able to reduce by the integrated package such as shown in Fig. 8(b).

Figs. 10 and 11 show the measurement result of bidirectional operation. The solid line shows the theoretical value calculated using (19) or (29). In Fig. 10(a), S_A adjusts the on-time $T_{\rm on}$ and $P_{\rm dd}$ flows from port A to port B. Both $P_{\rm dd}$ and $V_{\rm SA(p)}$ follow the theoretical values well. $P_{\rm dd}$ reaches 165 W at $T_{\rm on} = 1.3$ μs, and $V_{\rm SA(p)}$ reaches 120 V at this point. Fig. 10(b) shows the result of power control for the reverse direction by adjusting the on-time of S_B. $P_{\rm dd}$ flows from port B to port A and has the same profile as shown in Fig. 10(a).

Fig. 11 shows the measured efficiency and loss at $V_A = V_B$ $= 14$ V. The efficiency reaches a peak value of 92% at $P_{\rm dd} =$ ± 75 W as output and keeps over 90% in wide power range. Fifty percent of the total loss is dominated by the MOSFETs, with the remainder caused by the transformer. The resonant capacitors have small loss caused by the in ESR. If the circuit has stray inductance L_s next to the drain or source terminal of the MOSFET, turn-off current $i_{\rm off}$ causes additional loss $1/2 L_s I_{\rm off}^2$. In the MagCap circuit, $I_{\rm off}$ varies by the timing of the turn-off because of the ringing shown in the period T_b in Fig. 9. This effect is considered as one of the reasons for several efficiency pockets such as $P_{\rm out} = \pm 100$ W.

Regarding future extensions of this work, the GaN FET is feasible for increasing both the circuit power density and efficiency. This device achieves low resistance for high voltage with less effect for gate drive loss at high frequency, and the small device footprint helps in the design of a low stray inductance layout. Fig. 12 shows the estimated Pareto curve of the MagCap circuit by means of a GaN FET at $P_{\rm dd} = 150$ W. Table IV shows the sweep setting for this simulation. The heat sink volume is excluded from this study, and the transformer core and winding use the same material as the prototype. The operating frequency $f'_{\rm sw}$ is swept by the value of $C_1 = C_2$ and L_l, and number of switches D_p is also varied. For example, $D_p = 4$ means that the MagCap circuit uses same number of MOSFETs as the DAB. The volume or area of the components that have frequency dependence is estimated by the following rules. The volume of the transformer $V'_{\rm tr}$ is estimated based on the frequency ratio from the prototype, and it is regulated by the flux density of the transformer. The filter capacitor area $A'_{\rm cf}$ is determined by the regulation of the voltage ripple $V_{\rm ripple} \leq 0.2$ V. The power

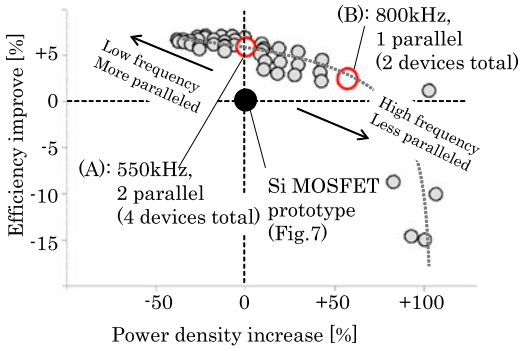

Fig. 12. Performance improvement estimation by GaN FET.

TABLE IV
SPECIFICATIONS OF THE EXPERIMENTAL CIRCUIT

	Si prototype	GaN estimation
Paralleled MOSFET #	1	$D_p = 1$ to 4
Operating frequency	$f_{\rm sw} = 550$ kHz	380 kHz $\le f'_{\rm sw} \le 1.5$ MHz
Density of PCB	$\rho = 0.65$ (use top layer only)	same as Si prototype
Flux density of transformer	50 mT	same as Si prototype
Voltage ripple of input capacitor	0.2 V	same as Si prototype
MOSFET (area)	6×5 mm$^2 \times 2$	2.5×4 mm$^2 \times 2 \times D_p$
Gate driver(area)	12×4 mm$^2 \times 2$	2×2 mm$^2 \times 2 \times D_p$
Transformer (volume)	$V_{\rm tr} = 10 \times 10$ mm^2	$V'_{\rm tr} = V_{\rm tr} \times f_{\rm sw}/f'_{\rm sw}$
Filter (area)	$A_{\rm Cf} = 8 \times 4$ mm$^2 \times 2$	$A'_{\rm Cf} = A_{\rm Cf} \times C'_f/C_f$
Capacitor (area)	$A_{\rm Cres} = 3.2 \times 0.5$ mm$^2 \times 2$	$A'_{\rm Cres} = A_{\rm Cres} \times C'_1/C_1$
Terminal (area)	5×20 mm$^2 \times 2$	same as Si prototype
Board height	$h_b = 2$ mm	same as Si prototype
Component height	$h_c = 2$ mm (from highest device)	same as Si prototype

density $V_{\rm sum}$ is calculated by the following equation:

$$V_{\rm sum} = \frac{h_b + h_c}{\rho} \sum (\text{area of devices}) + \text{transformer volume} \quad (33)$$

where ρ is the packaging density using only the top layer. As result, the GaN FET improves the efficiency approximately +6% in the same size as the Si case (point A) and increases the power density by +50% with 2.5% efficiency improvement (point B).

B. System Evaluation

Figs. 13 and 14 show the system evaluation result. Fig. 13(a) illustrates the circuit diagram, where two rechargeable power sources are connected to the MagCap. Port A of the MagCap connects to a 14 V battery emulator, and Port B connects to an EDLC (70 F, United Chemi-Con). A load R_v is connected to Port B as well and changes from open to 1.5 Ω. The controller provides pulse width modulation (PWM) signals to the gate drivers. Fig. 13(b) describes the control sequence of the system.

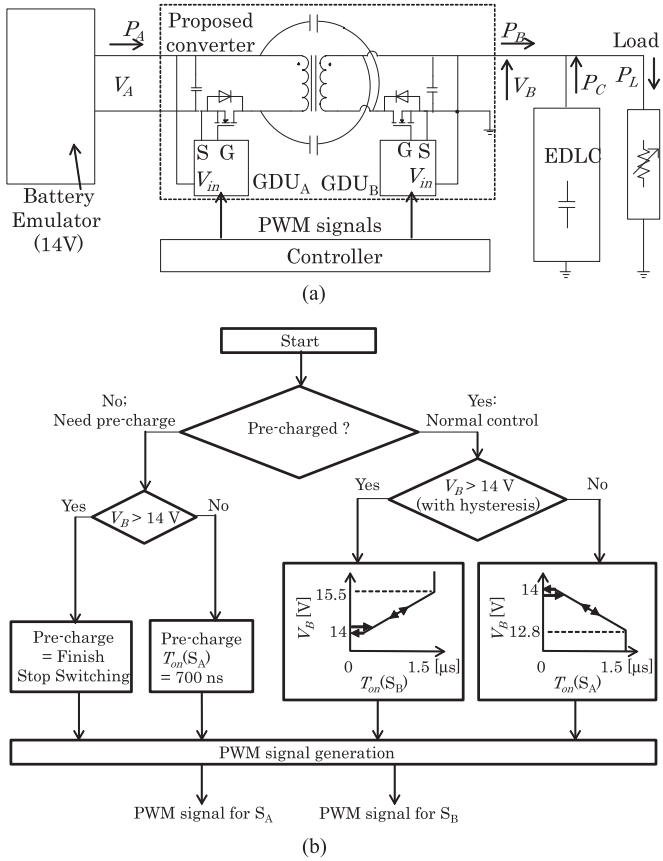

Fig. 13. System example with the proposed circuit. (a) System block diagram. (b) Flowchart of the droop control.

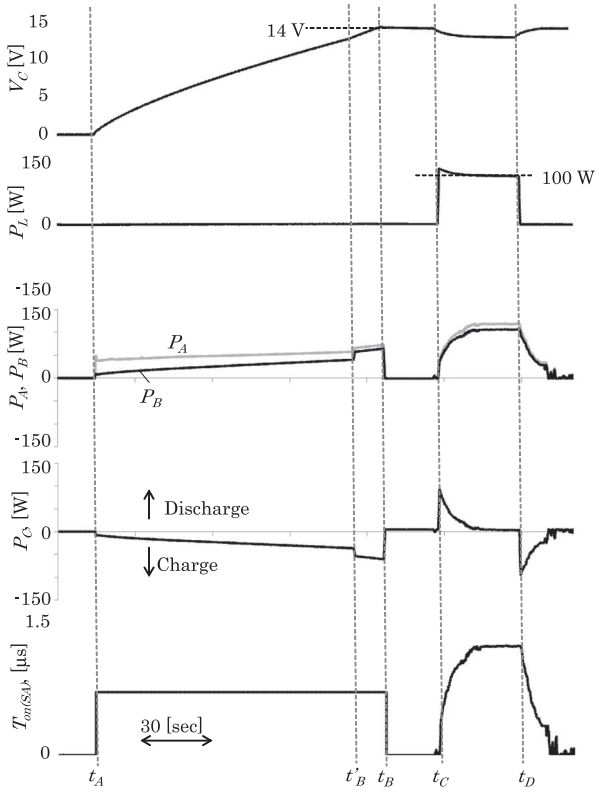

Fig. 14. Experimental results of the system example in Fig. 13.

This controller simply distributes the load power to both of the energy sources. The average power is distributed to the battery, and the EDLC deals with the transient power. The controller has a simple droop map, which uses the EDLC voltage V_B as reference, and adjusting $T_{\rm on}$ of one of the switches controls the battery power P_A bidirectionally, as shown in Fig. 10. When $V_B \leq 14\,\mathrm{V}$, the controller adjusts $T_{\rm on(SA)}$ to pull the battery power. On the other hand, the controller adjusts $T_{\rm on(SB)}$ when $V_B \geq 14\,\mathrm{V}$ to pull the EDLC power. Maximum on-time is set at 1.3 μs, which provides 150-W power transfer approximately, and the map sets a 0.15-V hysteresis window at 14 V to remove chattering. In this evaluation, a precharge sequence is added for initializing the droop system.

Fig. 14 shows the experimental results of the system utilization. At $t = t_A$, the system starts the precharge sequence of the EDLC. The on-time of the MOSFET $\mathrm{S_A}$ sets as $T_{\rm on(SA)} =$ 700 ns, and the MagCap charges the EDLC by using battery power. At $t = t'_B$, the gate driver $\mathrm{GDU_B}$ deactivates the under voltage lock out function and $\mathrm{S_B}$ can operate synchronous rectification. This delivers better efficiency and increases charging power.

When the EDLC voltage reaches $V_B = 14$ V at $t = t_B$, the system changes control mode to the normal control mode. The load R_v turns ON at $t = t_C$; the EDLC provides the transient power directly and drops its voltage. Then, the MagCap adjusts $T_{\rm on(SA)}$ by the change of V_B and increases the battery power P_A. At the steady state, the battery provides all of load power through the MagCap. The EDLC voltage reaches $V_B = 13.2$ V and on-time of $\mathrm{S_A}$ reaches $T_{\rm on(SA)} = 1.2$ μs. After the system turns OFF the load at $t = t_D$, the MagCap recovers the EDLC voltage to 14 V. Through this experiment, it is verified that the MagCap is capable of handling a wide voltage difference between the primary and secondary, and distributing dc grid power by using a simple droop controller, which is able to arrange the distribution strategy easily by modifying the V_B–$T_{\rm on}$ droop curve. For example, the MagCap is able to distribute the charging power for the battery and EDLC by adjusting the on-time of $\mathrm{GDU_B}$, when the system connects to a regenerative load such as a motor.

V. Conclusion

This paper has described a bidirectional dc–dc converter for dc distribution systems, with the idea of a magnetic and capacitive hybrid power transfer topology. Experimental results showed the functionally of bidirectional power control between isolated sources and soft switching using a small number of components. With such simplicity and high functionality, the proposed circuit enables a variety of applications for dc electric power systems in an age of increasing importance for renewable energy and energy storage.

References

[1] W. Zhang, D. Dong, I. Cvetkovic, F. C. Lee, and D. Boroyevich, "Lithium-based energy storage management for DC distributed renewable energy system," in *Proc. IEEE Energy Convers. Congr. Expo.*, 2011, pp. 3270–3277.

[2] J. P. Barton and D. G. Infield, "Energy storage and its use with intermittent renewable energy," *IEEE Trans. Energy Convers.*, vol. 19, no. 2, pp. 441–448, Jun. 2004.

[3] S. Sasaki, "Toyota's newly developed hybrid powertrain," in *Proc. 10th Int. Symp. Power Semicond. Devices ICs*, 1998, pp. 17–22.

[4] K. Snyder, X. Yang, and T. Miller, "Hybrid vehicle battery technology—The transition from NiMH to Li-ion," SAE Tech. Paper 2009-01-1385, 2009.

[5] J. G. Kassakian, "Automotive electrical systems—The power electronics market of the future," in *Proc. Appl. Power Electron. Conf.*, 2000, vol. 1, pp. 3–9.

[6] H. Yoo *et al.*, "System integration and power-flow management for a series hybrid electric vehicle using supercapacitors and batteries, *IEEE Trans. Ind. Appl.*, vol. 44, no. 1, pp. 108–114, Jan./Feb. 2008.

[7] F. Z. Peng, H. Li, G.-J. Su, and S. L. Jack, "A new ZVS bidirectional DC-DC converter for fuel cell and battery application," *IEEE Trans. Power Electron.*, vol. 19, no. 1, pp. 54–65, Jan. 2004.

[8] H. Tao *et al.*, "Multi-input bidirectional DC-DC converter combining DC-link and magnetic-coupling for fuel cell systems," in *Proc. IEEE Ind. Appl. Conf.*, 2005, vol. 3, pp. 2021–2028.

[9] T. Furukawa *et al.*, "Automobile efficiency improvements using electrochemical capacitor energy storage," in *Proc. World Electr. Veh. Symp. Exhib.*, 2013, pp. 1–6.

[10] S. Ziaeinejad *et al.*, "Design of a fuel cell-based battery extender auxiliary power unit for a vehicular microgrid," in *Proc. 40th Annu. Conf. IEEE Ind. Electron. Soc.*, 2014, pp. 3948–3954.

[11] S. Inoue and H. Akagi, "A bi-directional DC/DC converter for an energy storage system," in *Proc. Appl. Power Electron. Conf.*, 2007, pp. 761–767.

[12] J. Biela *et al.*, "Bi-directional isolated DC-DC converter for next-generation power distribution—Comparison of converters using Si and SiC devices," *IEEJ Trans. Ind. Appl.*, vol. 128, no. 7, pp. 901–909, 2008.

[13] U. Badstuebner, J. Biela, and J. W. Kolar, "Design of a 99%-efficient, 5kW, phase-shift PWM DC-DC converter for telecom applications," in *Proc. 25th Annu. IEEE Appl. Power Electron. Conf.*, 2010, pp. 773–780.

[14] C. Zhao, S. D. Round, and J. W. Kolar, "An isolated three-port bidirectional DC-DC converter with decoupled power flow management," *IEEE Trans. Power Electron.*, vol. 23, no. 5, pp. 2443–2453, Sep. 2008.

[15] A. A. Aboulnaga and A. Emadi, "High performance bidirectional Cuk converter for telecommunication systems," in *Proc. Telecommun. Energy Conf.*, 2004, pp. 182–189.

[16] B. R. Lin *et al.*, "Analysis of a zero voltage switching Cuk converter," in *Proc. 33rd Annu. Conf. IEEE Ind. Electron. Soc.*, 2007, pp. 1972–1977.

[17] T. Florencki and Y. Han, "High frequency resonant bidirectional SEPIC converter suitable for battery equalization and charger applications," in *Proc. IEEE Appl. Power Electron. Conf. Expo.*, 2014, pp. 2087–2092.

[18] G. Chen *et al.*, "Actively clamped bidirectional flyback converter," *IEEE Trans. Ind. Electron.*, vol. 47, no. 4, pp. 770–779, Aug. 2000.

[19] M. Muneeb Ur Rehman *et al.*, "Control of a series-input, parallel-output cell balancing system for electric vehicle battery packs," in *Proc. IEEE 16th Workshop Control Model. Power Electron.*, 2015, pp. 1–7.

[20] M. Muneeb Ur Rehman *et al.*, "Power electronics integration on battery cells," in *Proc. IEEE Appl. Power Electron. Conf. Expo.*, 2015, pp. 3318–3322.

[21] M. Tshukuda and I. Omura, "Demonstration of high output power density (30 W/cc) converter using 600V SiC-SBD and low impedance gate driver," in *Proc. Int. Power Electron. Conf.*, 2005, pp. 1184–1189.

[22] R. Simanjorang *et al.*, "A high output power density 400/400V isolated DC/DC converter with hybrid pair of SJ-MOSFET and SiC-SBD for power supply of data center," in *Proc. 25th Annu. IEEE Appl. Power Electron. Conf. Expo.*, 2010, pp. 648–653.

[23] B. Eckardt *et al.*, "Automotive powertrain DC/DC converter with 25kW/cc by using SiC diode," in *Proc. 4th Int. Conf. Integr. Power Syst.*, 2006, pp. 1–6.

[24] Y. Zhang *et al.*, " 100 MHz, 20 V, 90% efficient synchronous buck converter with integrated gate driver," in *Proc. IEEE Energy Convers. Congr. Expo.*, 2014, pp. 3664–3671.

[25] W. A. Tabisz and F. C. Lee, "Zero-voltage-switching multiresonant technique—A novel approach to improve performance of high-frequency quasi-resonant converters," *IEEE Trans. Power Electron.*, vol. 4, no. 4, pp. 194–204, Oct. 1989.

[26] J. Rivas *et al.*, "A very high frequency DCDC converter based on a class ϕ^2 resonant inverter," *IEEE Trans. Power Electron.*, vol. 26, no. 10, pp. 2980–2992, Oct. 2011.

[27] Z. U. Zahid *et al.*, "Design of bidirectional DC-DC resonant converter for vehicle-to-grid (V2G) applications," *IEEE Trans. Transp. Electrific.*, vol. 1, no. 3, pp. 1–14, Oct. 2015.
[28] H. Tao *et al.*, "Family of multiport bidirectional DC-DC converters," *Proc. Inst. Elect. Eng.—Electr. Power Appl.* vol. 153, no. 3, pp. 451–458, 2006.
[29] K. Ito *et al.*, "Analysis and design of a multiport converter using a magnetic coupling inductor technique," *IEEE Trans. Ind. Appl.*, vol. 51, no. 2, pp. 1713–1721, Mar./Apr. 2015.
[30] K. Ito *et al.*, "Loss estimation of an isolated three-port DC-DC converter for automotive applications," in *Proc. IEEE Energy Convers. Congr. Expo.*, 2015, pp. 3667–3673.
[31] S. Lim, J. Hansonet, J. A. Santiago-Gonzalez, and D. J. Perreault, "Capacitively-aided switching technique for high-frequency isolated bus converters," in *Proc. IEEE Appl. Power Electron. Conf. Expo.*, 2016, vol. 51, pp. 98–105.
[32] M. Muneeb, F. Zhang, R. Zane, and D. Maksimovic, "Design and control of an integrated BMS/DC-DC system for electric vehicles," in *Proc. IEEE 17th Workshop Control Model. Power Electron.*, 2016, pp. 1–7.
[33] N. Yousefpoo *et al.*, "Control of high-frequency isolated modular converter," *IEEE Trans. Ind. Appl.*, vol. 51, no. 6, pp. 4634–4641, Nov./Dec. 2015.

Masanori Ishigaki (M'14) received the B.S. degree in electrical engineering from Tokyo Metropolitan University, Tokyo, Japan, in 2005, and the M.S. degree in electrical and electronic engineering from Tokyo Institute of Technology, Tokyo, in 2007.

Since 2007, he has been with Toyota Central R&D Labs, Inc., Nagakute, Japan, and has been working for Electronics Research Department, Toyota Research Institute of North America, Ann Arbor, MI, USA, since 2014. His research interests include electrical systems for vehicle electronics and power converter circuits.

Mr. Ishigaki received the IPEC 2010 Second Prize Paper Award and the APEC 2012 Outstanding Presentation Award.

Jongwon Shin (M'15) received the B.S. and Ph.D. degrees in electrical engineering from Seoul National University, Seoul, South Korea, in 2006 and 2013, respectively.

He was a Postdoctoral Researcher at Virginia Polytechnic Institute and State University, Blacksburg, VA, USA, from 2013 to 2015. He is currently a Senior Research Scientist at Toyota Motor Engineering and Manufacturing North America, Ann Arbor, MI, USA. His research interests include power converter, energy management system, and power semiconductor packaging.

Ercan M. Dede (M'07) received the B.S. and Ph.D. degrees in mechanical engineering from the University of Michigan, Ann Arbor, MI, USA, in 1998 and 2007, respectively, and the M.S. degree in mechanical engineering from Stanford University, Stanford, CA, USA, in 2002.

He is currently a Manager in the Electronics Research Department, Toyota Research Institute of North America, Ann Arbor. His group conducts research on advanced vehicle electronics systems including power semiconductors, advanced circuits, packaging, and thermal management technology. He has more than 30 issued patents and has published more than 40 articles in archival journals and conference proceedings on topics related to design and structural optimization of thermal, mechanical, and electromagnetic systems. He is an author of a book entitled *Multiphysics Simulation: Electromechanical System Applications and Optimization* (London, U.K.: Springer, 2014).